AIAA 2003-4809

DEVELOPMENT OF EROSIVE BURNING MODELS FOR CFD PREDICTIONS OF SOLID ROCKET MOTOR INTERNAL ENVIRONMENTS

Qunzhen Wang
ATK Thiokol Propulsion
P.O. Box 707, M/S 252
Brigham City, UT 84302

39th AIAA/ASME/SAE/ASEE
Joint Propulsion Conference and Exhibit
July 20-23, 2003
Von Braun Civic Center/Huntsville, Alabama

Development of Erosive Burning Models for CFD Predictions of Solid Rocket Motor Internal Environment

Qunzhen Wang[§]

ATK Thiokol Propulsion Corp., Brigham City, UT

INTRODUCTION

It is widely known that the flow of combustion products at high velocity across a burning solid propellant surface leads to a significant increase in propellant burn rate over that obtained at the same pressure in the absence of crossflow[1-4]. This augmentation of burn rate by the flow of combustion gas across the propellant surface is referred to as erosive burning. Typically, erosive burning is only present during early burn for motors with small port-to-throat area ratio. Nevertheless, it is very important to take into account the effect of erosive burning in order to accurately predict motor performance. If the erosive burning effect is not properly accounted for in the design process, rocket failure may occur due to early exposure of some rocket motor parts to the hot combustion products and/or overpressurization immediately following ignition.

The most accurate erosive burning models are those modeling the detailed propellant burning process.[5] Ideally, these mechanistic models should be used in a three-dimensional transient computational fluid dynamics (CFD) simulation where the conservation laws of mass, momentum, energy, and multispecies are solved together with models of turbulence, combustion, and multiphase flow to predict the solid rocket motor internal environment. However, these types of simulations are very CPU time consuming and, thus, not suitable in the near future. As a result, most CFD simulations performed so far for the space shuttle reusable solid rocket motor (RSRM) and similar motors assume that the flow is steady while no combustion model is used and no species equations are solved.

Other types of erosive burning models are based on flow parameters such as pressure and Mach number at the bore centerline. For example, the Sanderholm model[3-4] has been widely used in one-dimensional ballistic codes. This empirical model divides the flow into three regions and calculates the propellant burn rate as follows. In the base burning region

$$r = ap^n \quad for \quad M \le M_{c1} \quad (1)$$

In the erosive burning region

$$r = 0.0093(MP)^{0.71}\left(\frac{1.2}{D_h}\right)^{0.2} \quad for \quad M \ge M_{c2} \quad (2)$$

In the transitional region

$$\frac{r}{ap^n} = \left(\frac{M}{M_{c1}}\right)^{\exp}\left(\frac{1.2}{D_h}\right)^{0.2} \quad for \quad M_{c1} < M < M_{c2} \quad (3)$$

where r is the burn rate, a and n are propellant dependent constants, D_h is the bore diameter, and p and M are the static pressure and Mach number at the centerline, respectively. Usually, the critical Mach number M_{c1} is about 0.07 and M_{c2} is about 0.5.

The empirical models such as the Sanderholm model were developed from static tests of very small size motors. When these models were applied to very large motors such as RSRM, however, the predicted pressure was much larger than the measured value, indicating that the effect of erosive burning is overpredicted. Therefore, these models were modified by introducing a scaling factor based on the motor bore hydraulic diameter to match the measured data.

The objective of this work is to develop erosive burning models that do not depend on the size of the motor. Since the propellant burning process is a local phenomenon occurring near the surface of the solid propellant, it makes sense to correlate the erosive burning ratio, which is defined as the ratio of burn rate with and without erosive burning, or erosive burning

[§]Sr. Principal Engineer, Gas Dynamics, AIAA member

difference, which is the increase in propellant burn rate due to erosive burning, with some local flow parameters at the propellant surface. In this work, the velocity gradient at the propellant surface du/dy, where u is the velocity parallel to the surface while y is the coordinate direction normal to the surface, is chosen as the local flow parameter. Furthermore, Reynolds analogy suggests that the heat transfer rate from gas to propellant is proportional to $du/dy/U$, where U is the centerline mean velocity of the gas. Since erosive burning is mainly caused by heat transfer to the propellant, erosive burning models are also developed in this work by assuming power law relationships exist between the erosive burning ratio or erosive burning difference and the local velocity gradient divided by the centerline velocity.

The pressure and propellant surface locations at different times measured in the 5 inch CP tandem motor testing[6] using ultra-sonic techniques are applied in this work to develop CFD-based erosive burning models. The propellant burn rate is obtained from the measured propellant surface locations by linear curve fitting. Steady-state CFD simulations of the 5 inch CP tandem motor are performed at different times using this burn rate. The erosive burning ratio or erosive burning difference from the measurement is then correlated with the velocity gradient at the propellant surface or the velocity gradient divided by the centerline velocity from the CFD simulations.

The erosive burning models are developed based on the data from the 5 inch CP tandem motor, which has a small bore diameter. In order to validate the applicability of these models to large motors, they are applied to CFD simulations of the following motors with different sizes: (1) 5 inch CP tandem motor with an initial bore diameter of 2 in; (2) Castor IVA-XL with a bore diameter of about 10 in; (3) Castor IVB with a bore diameter of about 10 in; (4) RSRM with a bore diameter of about 60 in; and (5) RSRM five segment engineering test motor No. 3 (ETM-3)[7] with a bore diameter of about 60 in. The predicted pressure is compared with the available measured data and the increase of headend pressure due to erosive burning is discussed in detail in this paper.

CFD APPROACH

The general-purpose CFD code SHARP[8-11] is used for all the CFD simulations shown in this paper. SHARP, which has been applied to internal flow simulations of various motors at ATK Thiokol Propulsion, is a density based flow solver where the conservation equations of mass, momentum and energy are solved on structured grids with multi-block topologies using a finite volume approach. The two-equation k-ε turbulence model is applied to take the effect of turbulent flow into account by solving additional transport equations of turbulent kinetic energy and dissipation rate.

In all CFD results shown in this paper, the flow is assumed to be steady state and 2D axisymmetric. The 3D fin regions of some motors are taken into account by adjusting the burn rate coefficient such that the total mass flow rate at the propellant surface is modeled correctly. The ratio of turbulence viscosity to laminar viscosity is limited to 10,000. It was also assumed that the combustion gas is a single-phase, chemically frozen, calorically perfect gas. That is, the fluid is assumed to be a homogeneous mixture of gas and particles with an equivalent molecular weight while no combustion model is applied and no real gas effect is taken into account.

The mass inflow boundary condition is applied at all propellant surfaces, where the mass flow rate is either specified or obtained from

$$\dot{m} = r\rho_s A \qquad (4)$$

where r is the propellant burn rate, ρ_s is the density of the propellant and A is the surface area. For simulations with erosive burning effect, the burn rate r is larger than the base burn rate ap^n. The normal velocity at the propellant surface is obtained by dividing the mass flux by the gas density while the tangential velocity is assumed to be zero. The gas temperature at the propellant surface is assumed to be the combustion flame temperature and the gas pressure at this boundary is calculated from the pressure at interior points. The grid spacing in the normal direction on the propellant surface for all the simulations shown in this paper is about 0.01 in. The velocity gradient at the propellant surface is calculated by dividing the tangential velocity of the first flow cell away from the propellant by the distance from the cell center to the propellant surface.

DEVELOPMENT OF EROSIVE BURNING MODELS

According to the Reynolds analogy, the momentum equation is similar to the energy equation and the friction coefficient is equal to the Stanton number:

$$\frac{\mu \frac{\partial u}{\partial y}}{\rho U^2} = \frac{h}{\rho U c_p} \qquad (5)$$

where ρ, μ, h, and c_p are the gas density, viscosity, heat transfer coefficient, and specific heat at constant pressure, respectively. The velocity U is the free-stream velocity for external boundary layer flows while it could be either the centerline velocity or the bulk velocity for internal flows. In this work, the centerline velocity is used. By rearranging equation (5), the heat transfer coefficient can then be written as

$$h = \mu c_p \frac{\partial u}{\partial y} \frac{1}{U} \qquad (6)$$

Since the viscosity and specific heat are assumed to be constants in this work, equation (6) indicates that the heat transfer coefficient is proportional to $du/dy/U$.

Since the propellant burning process is a local phenomenon occurring near the surface of the solid propellant, it makes sense to correlate the burn rate enhancement due to erosive burning with some local flow parameters at the propellant surface. The propellant burn rate enhancement can be quantified by the erosive burning ratio r/ap^n or the erosive burning difference $r-ap^n$, where r is the actual burn rate including the effect of erosive burning and ap^n is the base burn rate without erosive burning. In this paper, the local flow quantity is chosen as the velocity gradient du/dy at the propellant surface. Since erosive burning is mainly caused by the heat transfer from gas to propellants, it is also desirable to correlate the burn rate enhancement with a quantity proportional to the heat transfer coefficient such as the velocity gradient divided by centerline velocity $du/dy/U$.

Therefore, the following four erosive burning models are developed in this work by assuming power law relationships

$$\frac{r}{ap^n} = c_1 + c_2 \left(\frac{\partial u}{\partial y} \right)^{c_3} \qquad (7)$$

$$\frac{r}{ap^n} = c_1 + c_2 \left(\frac{\partial u}{\partial y} \frac{1}{U} \right)^{c_3} \qquad (8)$$

$$r - ap^n = c_1 + c_2 \left(\frac{\partial u}{\partial y} \right)^{c_3} \qquad (9)$$

$$r - ap^n = c_1 + c_2 \left(\frac{\partial u}{\partial y} \frac{1}{U} \right)^{c_3} \qquad (10)$$

The constants c_1, c_2, and c_3 are different in different models.

The pressure and propellant surface locations measured in the 5 inch CP tandem motor testing[6] using ultra-sonic techniques are applied to derive the values of c_1, c_2, and c_3 in the above equations. Specifically, the propellant burn rate for each segment is obtained from the measured propellant surface locations by linear curve fitting. Then the erosive burning ratio r/ap^n and the erosive burning difference $r-ap^n$ are calculated using this burn rate and measured pressure. Next, du/dy and $du/dy/U$ at the center of each segment are obtained from steady-state CFD simulations of the 5 inch CP tandem motor at different times. Finally, the constants c_1, c_2, and c_3 are obtained by curving fitting of the erosive burning ratio or erosive burning difference with the velocity gradient at the propellant surface or the velocity gradient divided by the centerline velocity.

5 INCH CP TANDEM MOTOR TESTING

Details of the 5 inch CP tandem motor testing are discussed in Ref. 6, so only a brief overview is given here. Six 5 inch CP motors, each of which has a grain length of 9 in, bore diameter of 2 in, and a propellant web of 1.5 in, are assembled together to form a tandem motor. Ultra-sonic transducers are used to measure the propellant surface locations at the middle of each segment while pressures at the seven slots between segments are measured with Taber 206 gage. The following three different propellants are used in the 5 inch CP tandem motor testing: ETM-3, Castor (TP-H8299), and RSRM propellants. Only some results from the ETM-3 propellant testing are shown in this section.

The propellant surface positions for different segments near 0.14 sec are shown in Figure 1. It is evident that the data points are not exactly on a straight line, indicating that the burn rate calculated by linear curve fitting these data will depend on how many points are used.

Figure 2 shows the propellant burn rate at 0.14 sec obtained from linear curve fitting of the surface location data in Figure 1 using different number of data points. Since the ultra-sonic technique used to measure the surface locations acquires data every 0.02 sec, using three points to calculate the burn rate at 0.14 sec means the measured data at 0.12, 0.14, 0.16 sec are applied while seven points means the data at 0.08, 0.10, 0.12, 0.14, 0.16, 0.18 and 0.20 sec are used. As expected, the

overall trend is larger burn rate at later segments due to erosive burning. However, the burn rate using different number of points are very different at some segments, suggesting that there is some uncertainty in the ultrasonic measurements.
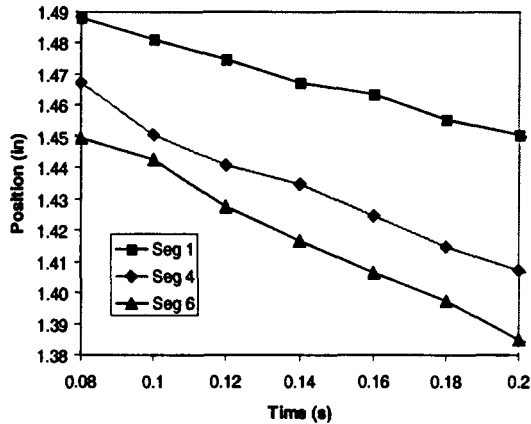

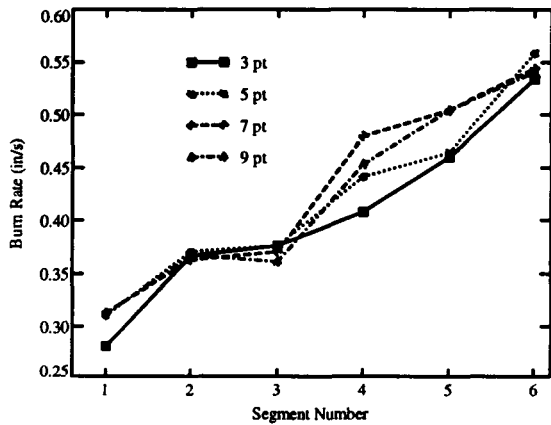*Figure 1: Measured location of propellant surfaces near 0.14 sec.*

Figure 2: Burn rate at 0.14 sec calculated from the measured location of propellant surfaces.

The erosive burning ratios r/ap^n at 0.14 sec obtained from the measured pressure and the burn rate in Figure 2 are shown in Figure 3. As expected, the erosive burning ratio is larger for downstream segments, indicating the effect of erosive burning is larger there. Moreover, the erosive burning ratio should be unity at the first segment since there is no erosive burning in this low velocity region. Figure 3 indicates that the erosive burning ratio is about 0.8 for the first segment at 0.14 sec. At this time, there is no apparent reason why the local burn rate in the forward segments would fall

below the static burn rate. It must be emphasized that there is significant data scatter in the measured surface position for all segments, especially early in motor burn. Later discussion will show that burn rate ratios less than 1.0 and burn rate differences less that 0.0 are not allowed by the erosive burning models developed herein.
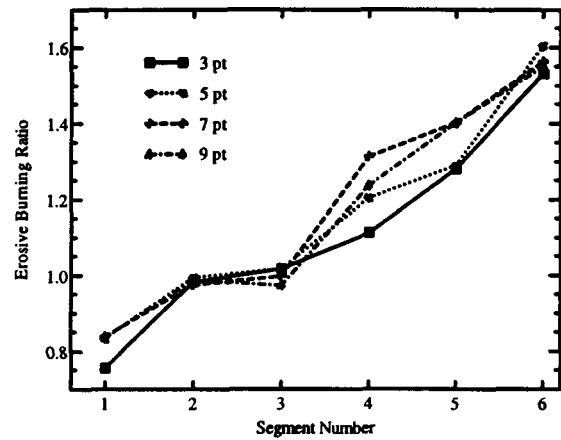
Figure 3: Erosive burning ratio at 0.14 sec calculated from the measured pressure and location of propellant surfaces.

The erosive burning differences $r-ap^n$ obtained from the measured pressure and the burn rate in Figure 2 at 0.14 sec are shown in Figure 4. As expected, the overall trend of the erosive burning difference is very similar to that of the erosive burning ratio and burn rate. The erosive burning difference should be zero at the first segment where there is no erosive burning but it is between −0.05 and −0.1 for the first segment at 0.14 sec.
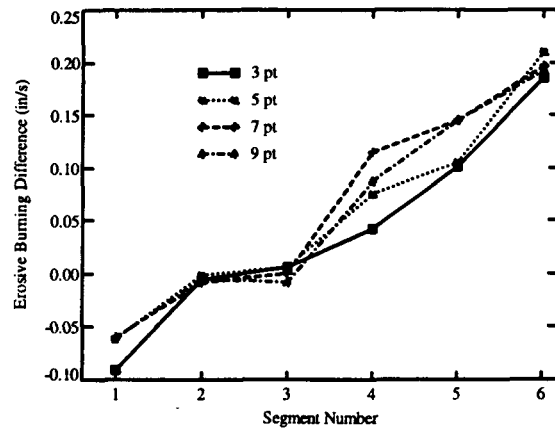

Figure 4: Erosive burning difference at 0.14 sec.

4

CFD RESULTS

In order to find the velocity gradient at propellant surfaces, steady state CFD calculations at 0.14, 0.3, 0.5, 0.7, 1.0, and 1.2 sec are performed using burn rates obtained from the measured propellant surface locations. Some results are shown in this section. Note that different grids are generated at different times since the geometry is time-dependent due to propellant burning.

ETM-3 Propellant

The predicted pressure using burn rates obtained from different number of points of the measured propellant location data at 0.14 sec are shown in Figure 5. Two identical motors with similar propellant are fired and the measured pressures from both motors are plotted in the figure. As expected, the predicted pressure is affected by the number of points used to calculate the burn rate. Overall, the predicted pressures are smaller than the measured ones.
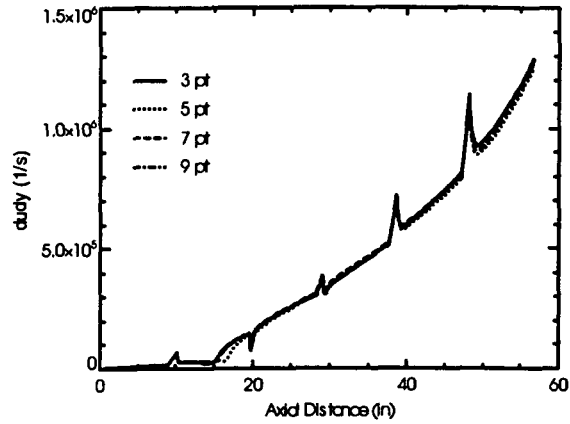

Figure 6: Predicted velocity gradient at the propellant surface using burn rates obtained from different number of points of the measured propellant location data at 0.14 sec.

Figure 5: Predicted pressure using burn rates obtained from different number of points of the measured propellant location data at 0.14 sec.
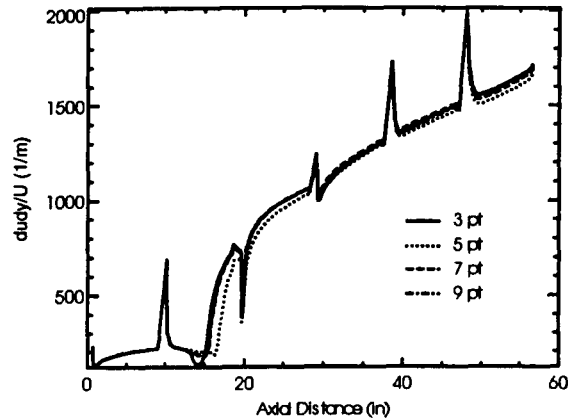

Figure 7: Predicted velocity gradient divided by centerline velocity using burn rates obtained from different number of points of the measured propellant location data at 0.14 sec.

The predicted velocity gradient at the propellant surface and velocity gradient divided by centerline velocity using burn rates obtained from different number of points of the measured propellant location data at 0.14 sec are shown in Figure 6 and Figure 7, respectively. Both of these quantities are much larger at later segments, indicating that they are good quantities to correlate the erosive burning enhancement with.

Figure 8 shows the predicted pressure using burn rates calculated with seven points at different times. Note that the burn rate has been increased by 2% to 5% in order to match the measured pressure since the measured pressure is believed to be more accurate than the burn rate calculated from the measured propellant surface locations. The predicted pressure agrees well with the measured data.
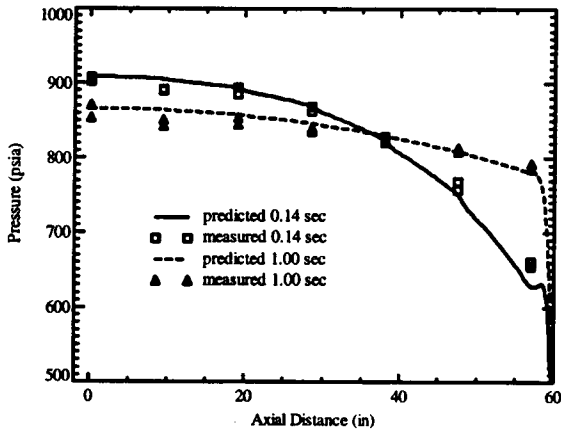
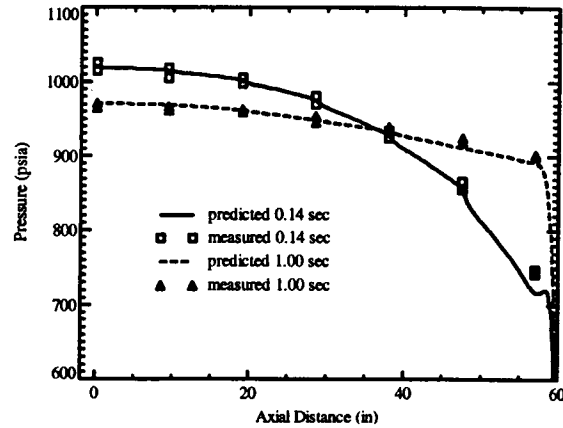*Figure 8: Predicted pressure for the tandem motor with ETM-3 propellant.*

Figure 10: Predicted pressure for the tandem motor with RSRM propellant.

Castor Propellant

The predicted pressures at different times for the tandem motor with Castor propellant are shown in Figure 9. Note that the burn rate has been reduced by 8% to 10%. The predicted pressure agrees well with the measured data.
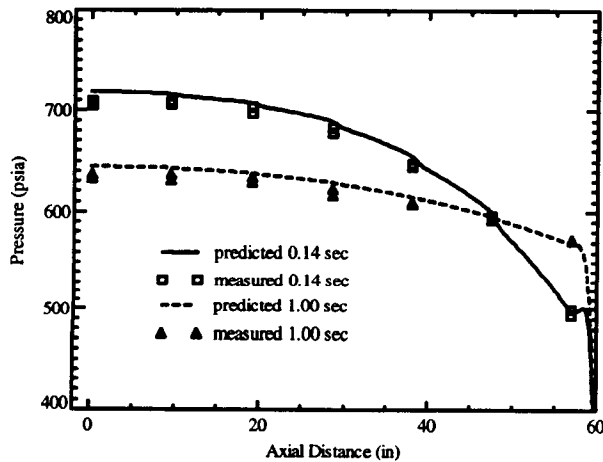

Figure 9: Predicted pressure for the tandem motor with Castor propellant.

RSRM Propellant

The predicted pressures at different times for the tandem motor with RSRM propellant are shown in Figure 10. Note that the burn rate has been reduced by 4% to 8%. The predicted pressure agrees very well with the measured data.

EROSIVE BURNING MODELS

The erosive burning ratio is plotted against the velocity gradient at the center of each segment in Figure 11 for ETM-3, Castor, as well as RSRM propellants. It is evident that the data is not very sensitive to the propellant and, thus, the erosive burning model developed in this work is independent of the propellant. Assuming that the propellant burn rate should never fall below the base rate (i.e., the erosive burning ratio is always larger than unity), model 1 is derived by curve fitting using a power law as

$$\frac{r}{ap^n} = \begin{cases} 1 & for \quad \frac{du}{dy} \le 1.29 \times 10^5 \\ 0.9237 + 3.289 \times 10^{-7} \left(\frac{du}{dy}\right)^{1.050} & for \quad \frac{du}{dy} > 1.29 \times 10^5 \end{cases} \quad (11)$$

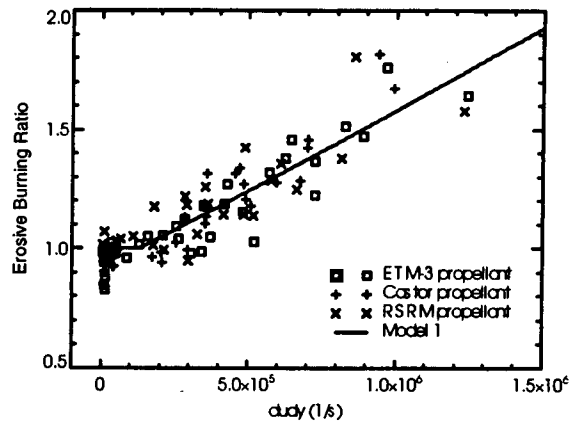The threshold for this model is $du/dy = 1.29 \times 10^5$ 1/s.

Figure 11: Erosive burning ratio vs. velocity gradient.

6

The erosive burning ratio is plotted against the velocity gradient divided by centerline velocity in Figure 12. Model 2 is derived by curve fitting using a power law as

$$\frac{r}{ap^n} = \begin{cases} 1 & for \quad \frac{du}{dy}\frac{1}{U} \le 622 \\ 0.9332 + 4.556\times10^{-4}\left(\frac{du}{dy}\frac{1}{U}\right)^{1.207} & for \quad \frac{du}{dy}\frac{1}{U} > 622 \quad (12) \end{cases}$$

The threshold for this model is $du/dy/U=622$ m^{-1}.
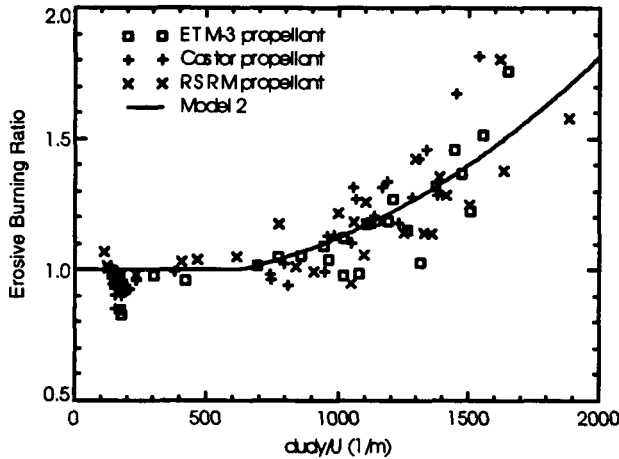
Figure 12: Erosive burning ratio vs. velocity gradient divided by centerline velocity.

The erosive burning difference is plotted against the velocity gradient in Figure 13. Similar to those shown in Figure 11 and Figure 12, the data is not very sensitive to the propellant and, thus, the erosive burning model developed here is independent of the propellant. Assuming that the erosive burning difference is always positive, model 3 is derived by curve fitting using a power law as

$$r - ap^n = \begin{cases} 0 & for \quad \frac{du}{dy} \le 1.38\times10^5 \\ -0.02781 + 5.631\times10^{-4}\left(\frac{du}{dy}\right)^{1.108} & for \quad \frac{du}{dy} > 1.38\times10^5 \quad (13) \end{cases}$$

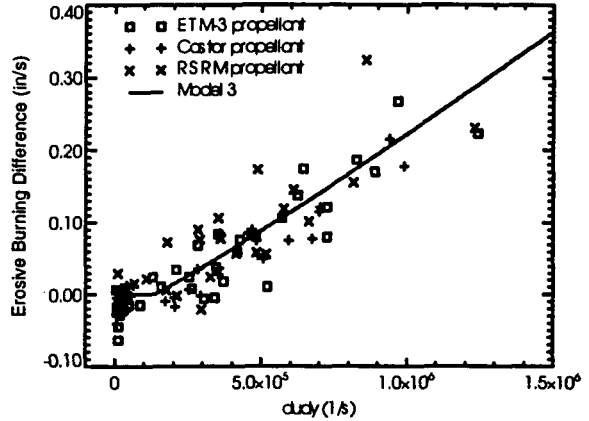The threshold for this model is $du/dy=1.38\times10^5$ 1/s.

Figure 13: Erosive burning difference vs. velocity gradient.

The erosive burning difference is plotted against the velocity gradient divided by centerline velocity in Figure 14. Model 4 is derived by curve fitting using a power law as

$$r - ap^n = \begin{cases} 0 & for \quad \frac{du}{dy}\frac{1}{U} \le 489 \\ -0.01129 + 5.444\times10^{-9}\left(\frac{du}{dy}\frac{1}{U}\right)^{2.349} & for \quad \frac{du}{dy}\frac{1}{U} > 489 \quad (14) \end{cases}$$

The threshold for this model is $du/dy/U=489$ m^{-1}.
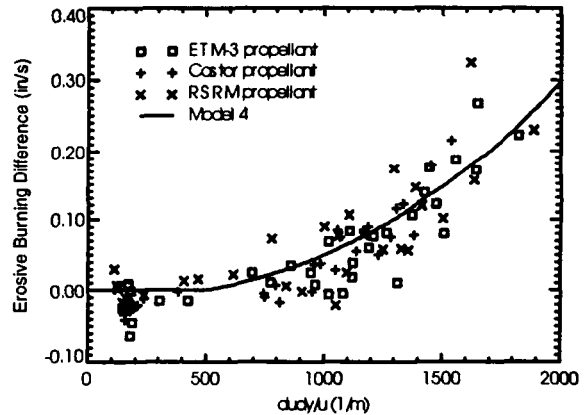

Figure 14: Erosive burning difference vs. velocity gradient divided by centerline velocity.

APPLICATION OF EROSIVE BURNING MODELS

The erosive burning models, equations (11) to (14), are developed using measured data from small size 5 inch CP tandem motor firings. In order to validate these models, they are applied to the CFD simulations of various motors with different sizes in this section. The predicted pressures with and without erosive burning models are compared with available data. Note that, while the burn rates from measured pressure and propellant surface locations such as those in Figure 2 are applied in the CFD simulations shown above, they are not used in the CFD results shown in this section. Instead, the propellant burn coefficient a and power n are specified and the burn rate is obtained from equations (11) to (14) using the calculated velocity gradient and mean centerline velocity.

5 INCH CP TANDEM MOTORS

Figure 15 and Figure 16 show the predicted pressure distribution with and without erosive burning models, together with the measured data, for the 5 inch CP tandem motor with ETM-3 propellant at 0.14 sec and 1.0 sec, respectively. It is evident that the predicted pressure is much smaller than the measured data if no erosive burning model is applied whereas the agreement is much better if erosive burning models are used. Erosive burning increases the headend pressure by about 150 psi at 0.14 sec and 60 psi at 1.0 sec. Results from the Castor propellant and RSRM propellant are similar and, thus, are not shown here.
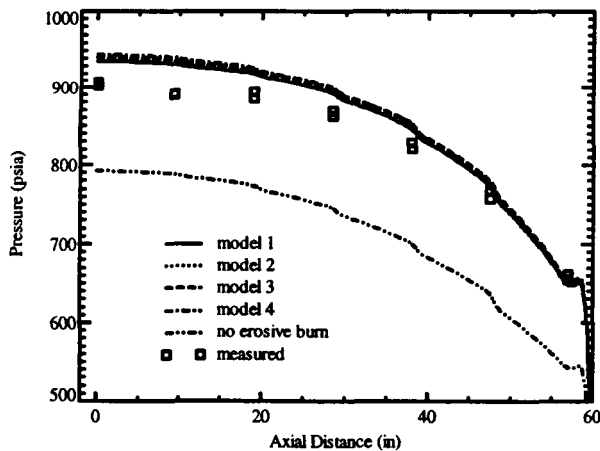

Figure 16: Comparison of pressure distribution with and without erosive burning models for the 5 inch CP tandem motor at 1.0 sec.
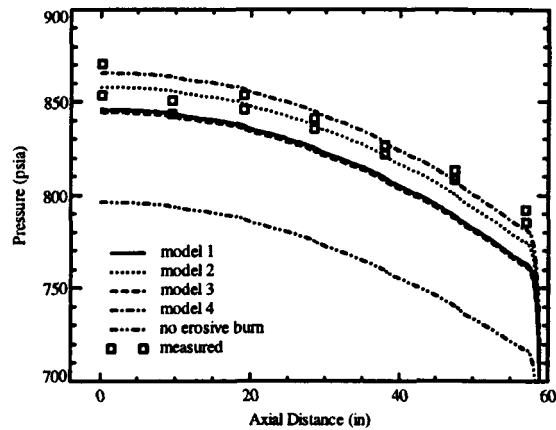
CASTOR IVA-XL

Figure 17 shows the predicted pressure distributions with and without erosive burning models for Castor IVA-XL. The headend pressure increases about 70 psi with these models. The predicted headend pressure with erosive burning is close to the measured value of 760 whereas that without erosive burning is much smaller.
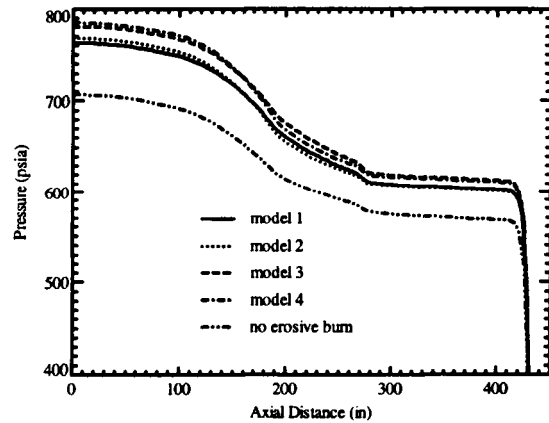

Figure 17: Comparison of pressure distribution with and without erosive burning for Castor IVA-XL.

CASTOR IVB

Figure 18 shows the predicted pressure distributions with and without the erosive burning models for Castor IVB. The headend pressure increases about 60 psi with

Figure 15: Comparison of pressure distribution with and without erosive burning models for the 5 inch CP tandem motor at 0.14 sec.
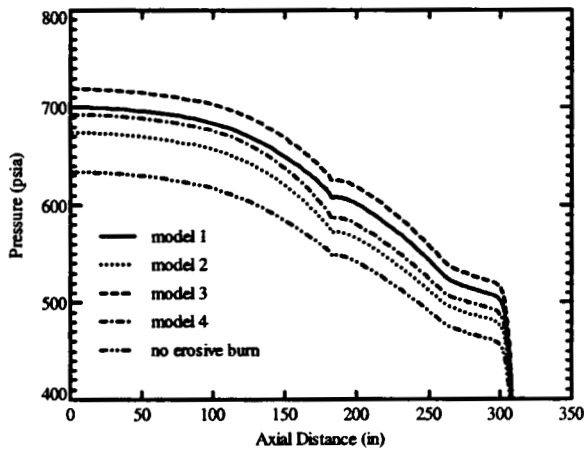
these models.

Figure 18: Comparison of pressure distribution with and without erosive burning for Castor IVB.

RSRM

The predicted velocity gradient at the propellant surfaces and the velocity gradient divided by centerline velocity are compared with the threshold values of the erosive burning models in Figure 19 and Figure 20, respectively. At 20 sec, the velocity gradient and the velocity gradient divided by centerline velocity are smaller than the threshold values at all locations, indicating that no erosive burning occurs at this time. At 1 sec, however, the propellant surfaces of the aft-center segment and near the slots between segments have velocity gradient larger than the threshold values, but most of the propellants have smaller velocity gradient. Therefore, model 1 and 3 will increase the headend pressure at 1 sec compared to that without erosive burning models, but the increase should be small. The velocity gradient divided by centerline velocity at 1 sec are smaller than the thresholds for all flow cells, so the predicted pressures using model 2 and 4 should be identical to that with no erosive burning models.

Figure 21 shows the predicted pressure distributions with and without erosive burning models, together with the measured data, for RSRM at 1.0 sec. As expected, the predicted pressures using model 2 and 4 are identical to that with no erosive burning models while the predicted headend pressure from model 1 and 3 are 2.7 psi and 1.6 psi higher, respectively. The small headend pressure increase due to erosive burning is consistent with most people's view that the RSRM has no or very little erosive burning.
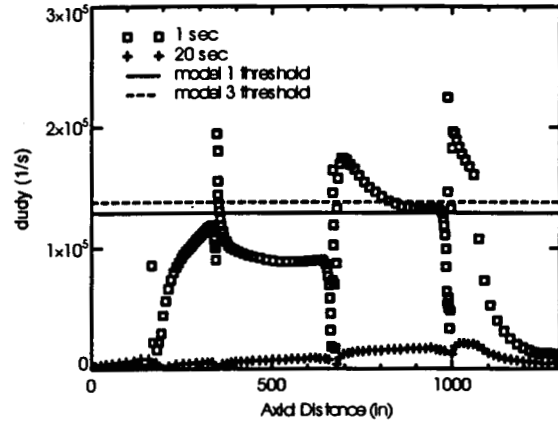

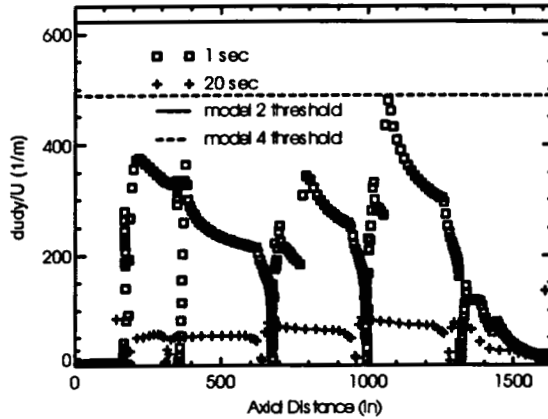*Figure 19: Predicted local velocity gradient for RSRM.*

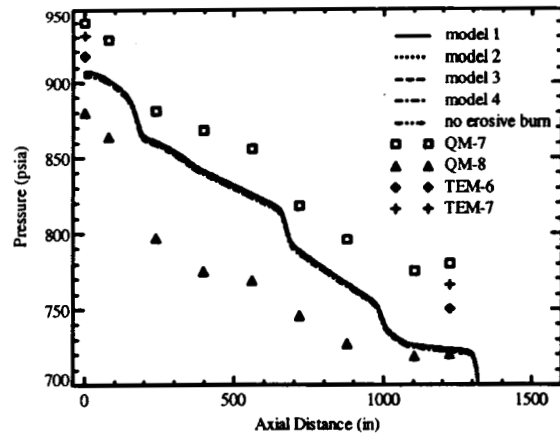*Figure 20: Predicted local velocity gradient divided by centerline velocity for RSRM.*

Figure 21: Comparison of pressure distribution with and without erosive burning models for RSRM.

9

ETM-3

The predicted velocity gradient at the propellant surfaces and the velocity gradient divided by centerline velocity are compared with the threshold values of the erosive burning models in Figure 22 and Figure 23, respectively. Similar to RSRM, the velocity gradient and the velocity gradient divided by centerline velocity at 20 sec are smaller than the threshold values at all locations, indicating that no erosive burning occurs at this time. At 1 sec, however, the propellant surfaces at most center segment and aft-center segment have velocity gradient larger than the threshold values, while those at the aft, forward and forward-center segments have smaller velocity gradient. Since the overall velocity gradient is larger, model 1 and 3 will increase the headend pressure at 1 sec more for ETM-3 than RSRM compared to that without erosive burning models. The velocity gradient divided by centerline velocity at 1 sec for ETM-3 are smaller than the thresholds, so the predicted pressures using model 2 and 4 should be identical to that with no erosive burning models.
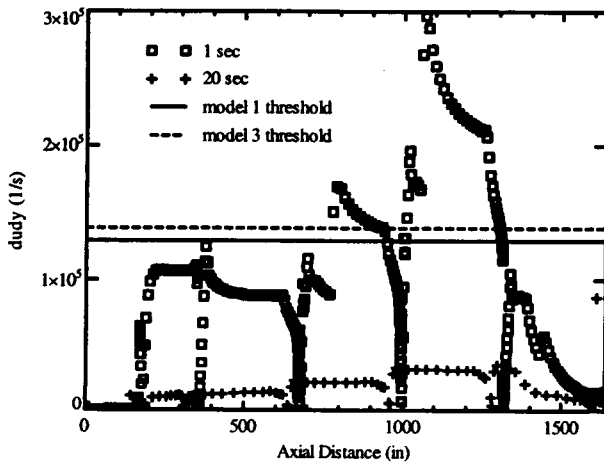

Figure 22: Comparison of local velocity gradient for ETM-3 with the thresholds in the erosive burning models.
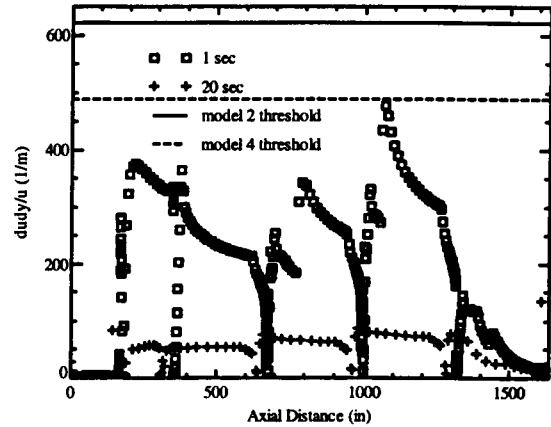

Figure 23: Comparison of local velocity gradient divided by centerline velocity for ETM-3 with the thresholds in the erosive burning models.

Figure 24 shows the predicted pressure distributions with and without erosive burning models for ETM-3 at 1.0 sec. The predicted pressures using model 2 and 4 are identical to that with no erosive burning models while the predicted headend pressure from model 1 and 3 are 8.5 psi and 7.3 psi higher, respectively. The bigger effect of erosive burning on ETM-3 compared to RSRM is also expected due to the smaller port-to-throat area ratio, which causes a larger gas velocity in the bore.
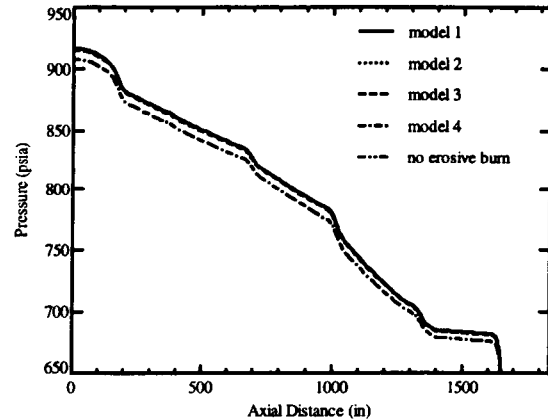

Figure 24: Comparison of predicted pressure distribution with and without erosive burning models for ETM-3.

CONCLUSIONS

Four erosive burning models, equations (11) to (14), are developed in this work by using a power law relationship to correlate (1) the erosive burning ratio and the local velocity gradient at propellant surfaces; (2) the erosive burning ratio and the velocity gradient divided by centerline velocity; (3) the erosive burning difference and the local velocity gradient at propellant surfaces; and (4) the erosive burning difference and the velocity gradient divided by centerline velocity. These models depend on the local velocity gradient at the propellant surface (or the velocity gradient divided by centerline velocity) only and, unlike other empirical models, are independent of the motor size. It was argued that, since the erosive burning is a local phenomenon occurring near the surface of the solid propellant, the erosive burning ratio should be independent of the bore diameter if it is correlated with some local flow parameters such as the velocity gradient at the propellant surface. This seems to be true considering the good results obtained by applying these models, which are developed from the small size 5 inch CP tandem motor testing, to CFD simulations of much bigger motors.

All four erosive burning models have been applied to 5 inch CP tandem motor, Castor IVA-XL, Castor IVB, RSRM, as well as ETM-3 and the results are compared with available measured data. Good overall agreement is obtained for all motors when erosive burning models are applied in the CFD predictions whereas the predicted pressure is much smaller if erosive burning model is not used. It was found that, due to erosive burning, the headend pressure increases by about 100-150 psi at 0.14 sec and 50-60 psi at 1.0 sec for the 5 inch CP tandem motor, 70 psi for Castor IVA-XL, and 60 psi for Castor IVB. The models based on velocity gradient divided by centerline velocity show no erosive burning for both ETM-3 and RSRM whereas those based on velocity gradient indicate that erosive burning increases the headend pressure by 1.6-2.7 psi for RSRM and 7.3-8.5 psi for ETM3 at 1 sec. The less than 2.7 psi headend pressure increase due to erosive burning for RSRM at 1 sec is consistent with most people's view that the RSRM has no or very little erosive burning. The bigger effect of erosive burning on ETM-3 at 1 sec compared to RSRM is also expected due to the smaller port-to-throat area ratio. For RSRM and ETM-3 at 20 sec, all models predict that there is no erosive burning at any locations.

REFERENCES

1. Razdan, M.K. and Kuo, K.K. 1984 "Erosive burning of solid propellants," in *Fundamentals of Solid-Propellant Combustion*, Edited by Kuo, K.K. and Summerfield, M., pp.515-598.
2. King, M.K. 1993 "Erosive burning of solid propellants," *Journal of Propulsion and Power*, Vol 9, pp.785-805.
3. Saderholm, C.A. 1964 "A characterization of erosive burning for composite H-series propellant," presented at *AIAA Solid Propellant Rocket Conference*, January 29-31, 1964.
4. Saderholm, C.A. 1972 "Combustion mechanisms of fuel rich propellants in flow fields," *AIAA Paper* 72-1145.
5. Yang, V. and Zarko, V.E. 1995 (eds.) "Solid-propellant rocket motor interior ballistics and combustion of energetic materials," *Journal of Propulsion and Power*, Vol. 11, No. 4, July 1995.
6. Furfaro, J. 2003 "Erosive burning study utilizing ultrasonic measurement techniques," *AIAA Paper* 2003-4806.
7. Huppi, H., Tobias, M. and Seile, J. 2003 "Enhanced large solid rocket motor understanding through performance margin testing – RSRM Five Segment Engineering Test Motor (ETM-3)," *AIAA Paper* 2003-4958.
8. Golafshani, M. and Loh, H.T. 1989 "Computation of two-phase viscous flow in solid rocket motors using a flux-split Eulerian-Lagrangian technique," *AIAA Paper* 89-2785.
9. Loh, H.T. and Golafshani, M. 1990 "Computation of viscous chemically reacting flows in hybrid rocket motors using an upwind LU-SSOR scheme," *AIAA Paper* 90-1570.
10. Loh, H.T., Smith-Kent, R., Perkins, F and Chwalowski, P. 1996 "Evaluation of aft skirt length effects on rocket motor base heat using computational fluid dynamics," *AIAA Paper* 96-2645.
11. Laubacher, B.A., Eaton, A.M., Pate, R.A., Wang, Q., Mathias, E.C. and Shipley, J.L. 1999 "Cold-flow simulation and CFD modeling of the space shuttle solid rocket motor nozzle joints," AIAA Paper 99-2793.

11
American Institute of Aeronautics and Astronautics